Effective area calibration of the Nuclear Spectroscopic Telescope Array

Kristin K. Madsen[a,b] **Karl Forster**[c] **Brian Grefenstette**[c] **Fiona A. Harrison**[c] **and Hiromasa Miyasaka**[c]

[a]NASA Goddard Space Flight Center, CRESST and X-ray Astrophysics Laboratory, Greenbelt, Maryland, United States

[b]University of Maryland, Department of Physics and Center for Space Science and Technology, Baltimore, Maryland, United States

[c]California Institute of Technology, Pasadena, California, United States

Abstract. We present here the updated calibration of the Nuclear Spectroscopic Telescope Array, which was performed using data on the Crab accumulated over the last nine years in orbit. The basis for this new calibration contains over 250 ks of focused Crab observations (imaged through the optics) and over 500 ks of stray-light (SL) Crab observations (not imaged through optics). We measured an epoch averaged spectrum of the SL Crab data and define a canonical Crab spectrum of $\Gamma = 2.103 \pm 0.001$ and $N = 9.69 \pm 0.02$ keV^{-1} cm^{-2} s^{-1} at 1 keV, which we use as our calibration standard. This calibration released in the Calibration Data Base update 20211020 provides significant updates to: (1) the detector absorption component, (2) the detector response function, and (3) the effective area vignetting function. The calibration improves agreement between FPMA and FPMB across detectors with a standard deviation of 1.7% for repeat observations between off-axis angles of 1′ to 4′. As a consequence of the measured SL observations, the absolute flux of the instrument has increased by 5% to 15%, with 5% below 1′ off-axis angle, 10% between 1 and 2′, and 15% above 4′. [DOI: 10.1117/1.JATIS.8.3.034003]

Keywords: Nuclear Spectroscopic Telescope Array; x-ray; satellite.

Paper 22038G received Mar. 25, 2022; accepted for publication Sep. 9, 2022; published online Sep. 29, 2022.

1 Introduction

The Nuclear Spectroscopic Telescope Array (NuSTAR) was launched in June 2012,[1] and it carries two co-aligned conical grazing incidence Wolter-I approximation[2] optics modules A and B (OMA and OMB) that focus onto two identical focal plane modules A and B (FPMA and FPMB). Each of these are composed of four solid state CdZnTe pixel detector arrays (enumerated Det0 through Det3). There are 133 shells in each optic, and the outer 43 shells are coated with a W/Si multilayer while the inner 90 shells are coated with Pt/C, limiting the highest efficient reflective x-ray energies to the Pt 78.4 keV K-edge.[3]

The instrument has been in orbit for nine years and the original effective area calibration, reported by Madsen et al.,[4] was performed during the first year and a half of operation. Based on the results from Toor and Seward[5] and the investigation by Kirsch et al.,[6] we calibrated against a canonical Crab standard of $\Gamma \equiv 2.1$ and $N \equiv 8.5$ keV^{-1} cm^{-2} s^{-1} at 1 keV. Then, in 2016, there was an update to the detector gain and a re-calibration of the detector absorption (DETABS) parameters, reported in Madsen et al.'s work[7] that necessitated a readjustment of the vignetting function. Both of these effective area and vignetting calibrations were generated the same way as the original calibration, which we name the off-axis angle weighting method, or "oaa-weighting" for short and summarize below. In August 2020 (and again updated in July 2021), we provided a correction of the multilayer insulation (MLI) absorption covering OMA because evidence

*Address all correspondence to Kristin K. Madsen, kmadsen@umbc.edu

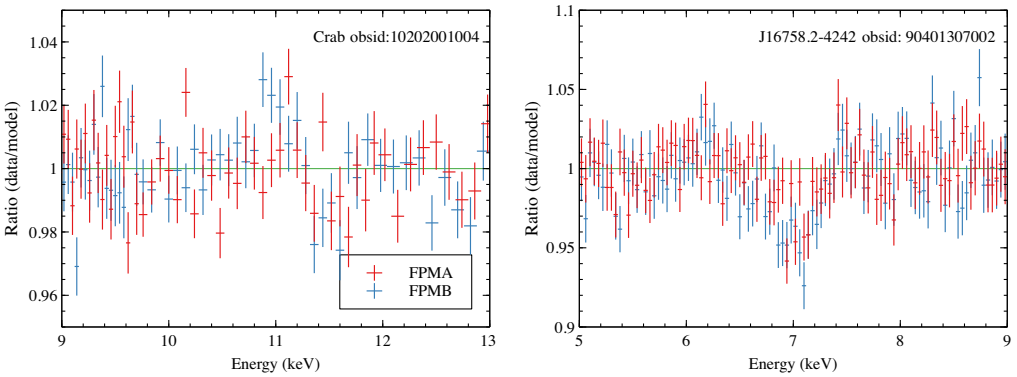

Fig. 1 Examples of absorption-like lines in the Crab at ∼11.2 keV, which is due to the Pt Lβ edge, and for J1658.2-4242 at ∼7.1 keV, which has no known reason except that the ARF has a feature right there that has been seen in one other source, and this could therefore still be of astrophysical origin.

indicated that the MLI had been ripped and now exposes part of the optic aperture of OMA directly to space.[8] This correction is independent of off-axis angle and is applied along with the DETABS as a multiplicative factor onto the ancillary response file (ARF).

The original calibration and its 2016 update has generally performed well, but over the years features have emerged when observing high signal to noise sources in addition to those mentioned above:

1. differences between FPMA and FPMB spectra at low energy due to incorrect DETABS values, large differences in spectra from different detectors on the same FPM, related to the same incorrect DETABS
2. low energy tails related to the detector response
3. absorption or line-like features in the spectrum related to the vignetting function.

These are not of a time dependent nature but are functions of specific off-axis angles and locations on the detector, which is why they became more apparent due to increased statistics and a larger pool of sources in which they were observed. We show a couple of examples of the line-like features in Fig. 1, and in many cases they are only on the 2% to 4% level, and therefore, hard to distinguish from astrophysical ones except when we can correlate to a response feature as in the case of the Pt *L*-edge complex between 11 and 12 keV. Very rarely do these features show up consistently, and although they motivated us to this re-calibration effort we were unsuccessful in consistently removing them.

Because the various components of the instrument response and their effects on the spectrum are interleaved, the re-calibration had to occur in a specific order. The calibration hinges upon the precise measurement of the stray-light (SL) Crab spectrum, and we first had to re-measure the correct DETABS coefficient and address the detector response below 5 keV. We did this with the SL Crab data and the details are presented in Sec. 5. Once those had been updated, we could proceed to the calibration of the telescope effective area and vignetting function using the focused Crab data, which is detailed in Sec. 6.

In the following sections, we will refer to the collection of four detector as a module, and when we discuss individual detectors, we will in short form designate them in the format Det0A, which would be Det0 on FPMA.

Readers interested only in the short short version should read Secs. 2, 4, 5.2.2, 5.2.3, 6.2, and 7.

2 NUSTARDAS and the CALDB

A detailed summary of NuSTAR Data Analysis Software and the High Energy Astrophysics Science Archive Research Center Calibration Data Base (CALDB) revisions can be found

Table 1 Version numbers.

Component	Internal version	Pre CALDB 20211020	CALDB 20211020
ARF vignetting	v9.5	v007	v008
RMF	v003	2010v002	2010v003
DETABS	v16	v003	v004

on the NuSTAR Science Opeartions Center (SOC) pages,[9] but we provide here a relevant summary for the analysis to be discussed.

Until now, the detector redistribution matrix file (RMF) has not changed since its initial release in August 14, 2013, and we refer to this RMF as 2010v002, which reflects its version number in the CALDB. As part of the preparation to update the RMF, an intermediate RMF was created, which is described in Sec. 5.2.3, and we refer to this RMF as v3.0. This is an internal version to the SOC and is not released to the CALDB. The final corrected RMF product that is released to the CALDB we refer to as v3.1. This appears in the 20211020 CALDB as 2010v003.

The mirror ARF, in particular the vignetting function, has undergone a couple of iterations since launch. The version upon which the corrections described in this paper are built originates from June 06, 2016. We refer to this vignetting function as v007, based on its revision number in the CALDB. The final corrected vignetting file to be released to the 20211020 CALDB we refer to as v008.

In June 06, 2016, we also released DETABS v003, and the new updated version from Table 3 released in the 20211020 CALDB we refer to as DETABS v004.

The version numbers are summarized in Table 1 for easy reference, and for all data reductions that use NUSTARDAS we use version v2.1.1.

3 NuSTAR Calibration Methodology

Instrumentation should preferably be understood by their ground calibration and only require additional in-orbit calibration to verify the ground results. Reality, however, has shown that instrumentation often requires additional adjustment. Sometimes this can be due to a process that happened after the ground calibration occurred, such as a time dependent contamination layer or detector gain shifts. But sometimes, the underlying physical process, or geometry, may not be known or too complex to accurately model at the time. For NuSTAR, the fundamental challenge in calibrating the optics resides in the complexities of the multilayer response.

There are 10 different multilayer design prescriptions[3] distributed across ∼3000 individual segments of glass, and although the theoretical responses of the recipes are known, and we know where each segment resides, during production variations occurred in the recipes. Since we did not measure the responses of all individual pieces, which are highly dependent on grazing incidence angle, we do not know the true response of each piece, and although the ground calibration was thorough[10–12] when applied to astrophysical data large residuals remained,[4] and it became necessary to calibrate the effective area of the NuSTAR optics against a standard candle once in orbit.

The most appropriate standard candle in existence for NuSTAR is the Crab. It is a center filled pulsar wind nebula (PWN) powered by a pulsar with a double peaked profile of period $P \sim 33$ ms, and it has served as the primary celestial calibration source for many hard x-ray instruments because of its brightness, relative stability, and simple power-law spectrum over 1 to 100 keV.[6] For NuSTAR in particular, its stability and brightness over the 3- to 80-keV band makes it superior to any other PWN and enables us to map out the vignetting function of the instrument in a relative short amount of time (one exposure is typically around 5 ks), which would not be possible with any other source in the available time allocation for calibration. With a point spread function of $\sim 1'$ the angular extent of the Crab has only a minor impact on NuSTAR as it remains centrally peaked.

The phase-averaged integrated spectrum of the Crab Nebula+Pulsar between 1 and 100 keV has been well-described by a power-law with a photon index of $\Gamma \sim 2.1$,[6] while above 100 keV, the hard x-ray instruments (INTEGRAL/SPI/ISGRI, CGRO) measure a softer index of $\Gamma \sim 2.20 - 2.25$. The exact location of the turnover is not well determined, and it appears gradual, estimated to occur somewhere between 50 and 120 keV.[13] Weisskopf et al.[14] did a study with RXTE/PCA, XMM-Newton, and ASCA, looking for deviations from a power-law in the 0.2- to 50-keV energy range, and concluded that within the precision of the available instrumentation there is no detectable bend in the phase-averaged integrated spectrum of the Crab. Measurements using NuSTAR SL data support these findings.[7]

The stability of the Crab has been tracked in great detail over the last decade, and during this period the flux has been observed to change by 7% across the 10- to 100-keV bandpass.[15] This variation is slow and the deviation in flux per year over the period it has been observed is on the order of ~3%. In NuSTARs lifetime, it has been particularly stable as shown in Fig. 16. The spectral index has also been observed to vary peak-to-peak by $\Delta\Gamma \sim 0.025$ in RXTE/PCA,[16] but, as with the flux variation, it is slow. On average, over the 16 years, the Crab has been observed, it has remained steadily at $\Gamma \sim 2.1$. In our calibration, we are unable to account for the intrinsic variations within the source over the time we observed it, and we must treat them as systematic. However, since the systematic errors of the instrument from repeated measurement are of a similar magnitude,[4] the intrinsic variability of the Crab is acceptable for our purpose.

3.1 *Vignetting Correction Function*

The task of the NuSTAR calibration is to compare the measured spectrum to the assumed Crab model. Mathematically, we model the detected counts in a given instrumental pulse height bin, $C(PI, \theta)$, according to the equation,

$$C(PI, \theta) = \int \frac{dN(E)}{dE} R(PI, E, \theta) \mathrm{d}E. \tag{1}$$

Here, $dN(E)/dE$ is the model differential photon spectrum of the observed target as a function of incident photon energy, E, and $R(PI, E, \theta)$ is the instrument response that captures the incident photon in a given pulse height bin, PI, at an off-axis angle, θ. In practice, this integral is approximated as a finite sum by sampling $R(PI, E, \theta)$ on a grid. The off-axis angle, θ, is the angle of incoming x-rays with respect to the optical axis of the telescope. As the optical axis moves with respect to the detector position during an observation, the modeled response is sampled on a finite time grid and then summed for a given exposure.

As is typical for x-ray astrophysical missions, the response matrix is divided into two components,

$$R(PI, E, \theta) = \mathrm{RMF}(PI, E) \circledast \mathrm{ARF}(E, \theta). \tag{2}$$

Here, $\mathrm{RMF}(PI, E)$ is known as the RMF, which contains detector quantum efficiency and resolution effects, and it is unitless (a fraction between 0 and 1, where a value of 1 indicates 100% quantum efficiency). The RMF will be discussed in greater detail in Sec. 5.2.3. The quantity $\mathrm{ARF}(E, \theta)$ is the ancillary response function, which captures the effective area of the optics as well as several other attenuation factors unique to NuSTAR:

$$\mathrm{ARF}(E, \theta) = A_o(E) \times V(E, \theta) \times \mathrm{DETABS}(E) \times \mathrm{GR}(E, \theta) \times \mathrm{AS}(E, \theta) \times \mathrm{Corr}(E, \theta). \tag{3}$$

Here, $A_0(E)$ is the modeled on-axis effective area of the mirror segments estimated from theoretical ray-tracing simulations, and $V(E, \theta)$ the geometric vignetting function, also based on ray-tracing simulations. The quantities DETABS, GR, and AS are the detector dead layer (DETABS) absorption (discussed in Sec. 5.2.1), ghost ray correction (GR), and aperture stop correction (AP). We do not concern ourselves with the GR and AP, and details on these components can be found in Madsen et al.'s work[4,17] For the ARF, $\mathrm{Corr}(E, \theta)$ is the empirically derived correction factor we want to obtain.

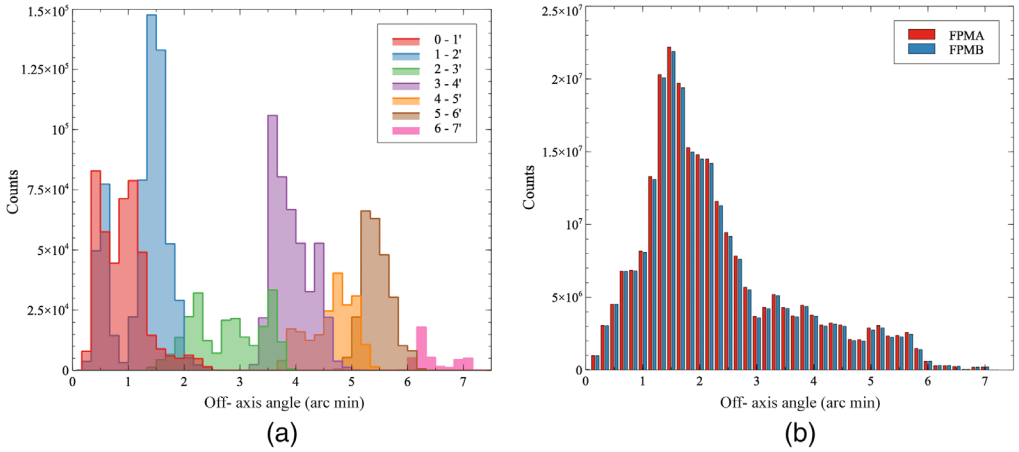

Fig. 2 (a) Histogram of the original binning of the oaa-weighting method using the 35 observations available at the time.[4] (b) New histogram of all 71 Crab observation listed in Table 6 sorted by off-axis angle in 10″ bins.

In practice, discovering the correction function $\mathrm{Corr}(E,\theta)$ involves taking numerous observations of the Crab at different off-axis angles. In this way, a grid of countrates at E and θ are obtained and can be used to interpolate the response at any desired point, where, obviously, the finer the grid the more accurate the function. With NuSTAR, however, obtaining such a data set is problematic.

The observatory has an optics bench and a focal plane bench separated by 10.14 m, which move relative to each other due to motions of the mast that connects them and causes the optical axis to travel across the FPMs by up to several arcminutes. This means that each observation samples a range of off-axis angles that is unique for that observation. In our original oaa-weighted method we calculated the mean off-axis angle for each observation and assigned the observations to 1 arc min bins: 0–1′, 1–2′,. . . , 6–7′. For each bin, the assigned observations were then combined, and a new off-axis angle for the combined dataset was calculated by weighting the individual off-axis angle distributions.

The issue with this method is obviously that the combined distributions are overlapping as shown in Fig. 2(a), and that the spectra are sampling a range of off-axis angles that go beyond the assigned bin. Also, because the bins were required to be large enough to accumulate enough statistics, our knowledge of what happened in between is poor. For this old dataset, Fig. 3(a) shows the effective area correction factor, $C(E,\theta)$ for energies 3.0, 10.1, and 46.3 keV. Although to first approximation the correlation appears linear as a function of off-axis angle, there is residual substructure clearly visible.

3.1.1 *New method: meta spectra*

To address the issues of the previous calibration, we devised a new method. The number of Crab observations has grown from the initial 39 to 71. With more than double the increase in exposure time this allows for a higher fidelity analysis than was previously available. The most important change is that we calculate the off-axis angle of each individual photon. Due to the extent of the Crab and the PSF, we do not measure the actual photon's position, but the off-axis angle of the source center at the time of the photon's arrival. In this manner, we can assign each photon to a specific off-axis angle bin without having overlapping distributions and the new histogram photons from the 71 observations sorted by off-axis angle can be seen in Fig. 3(b).

We use 10″ as the smallest subdivision, but also bin at 60″, which becomes useful for energies above 60 keV and large off-axis angles. We combine all observations from the same off-axis angle bin together in an epoch-mixed meta spectrum that we fit against the reference Crab model to obtain the correction for each 10″ bin. Figure 4 shows the ratio (data/model) of the meta spectra reduced with the original ARF v007, but with new adjustments to the DETABS and RMF, binned in 60″ for ease of viewing. Figure 5 shows the same ratio of the 100 to 200″ data

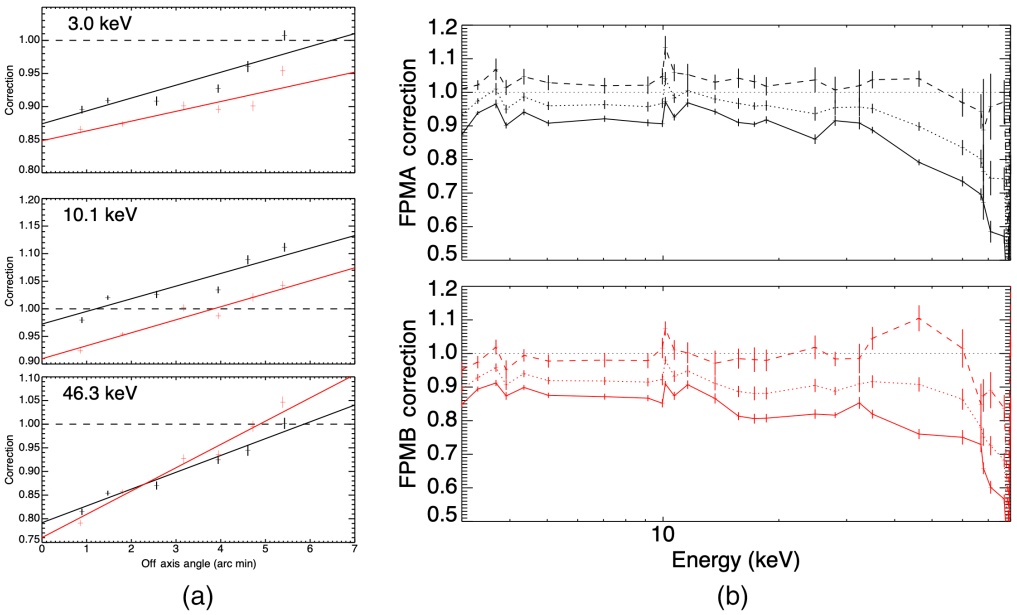

Fig. 3 Correction functions, Corr(θ, E), used to derive CALDB 20131223 presented in Madsen et al.[4] (a) The linear (in θ) function for selected energies. (b) Corr(θ, E) for offaxis angles 0′ (solid), 3′ (dotted), and 7′ (dashed).

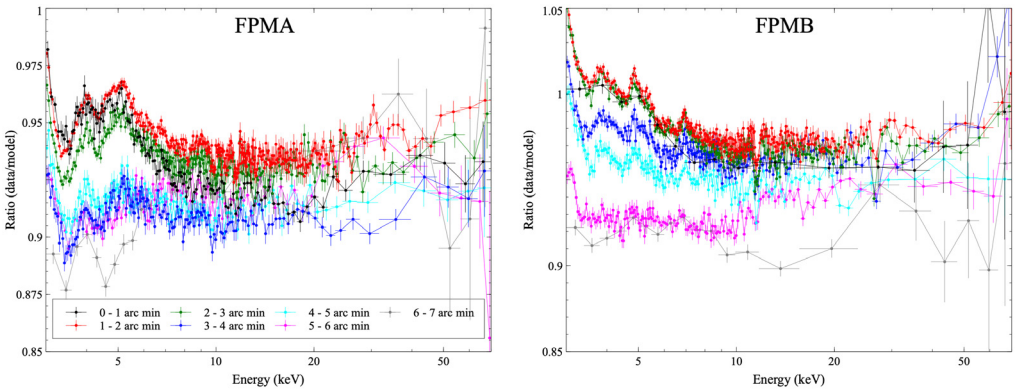

Fig. 4 Ratio of the data reduced with ARF v007, but with new DETABS parameters (see Sec. 5.2.1) and RMF v3.1, to the Crab model in 1 arc min bins for FPMA and FPMB. This shows that the flux increase will be largest for larger off-axis angles and low energies.

in 10″ bins. Systematic, non-linear changes across the sub-arcminute bin can be observed, but the largest deviations from the Crab spectrum shown here, particularly at low energies, are far more severe looking than would be obtained with the original responses. The reason for this is that the adjustments to the DETABS parameters and the new RMF, to be discussed in Sec. 5, must be included in the data reduction before deriving the corrections to the vignetting function itself, and therefore, these ratio plots indicate the level to which the detector related instrument terms were previously incorrectly included into the vignetting function. In short, much of what follows is to disentangle detector related effects from the vignetting function.

4 Crab Spectrum

In the NuSTAR band the Crab spectrum is well represented by a powerlaw with galactic absorption expressed in XSPEC nomenclature as tbabs × powerlaw. Toor and Seward[5] discussed the Crab in the context of a steady calibration source and measured the normalization and powerlaw

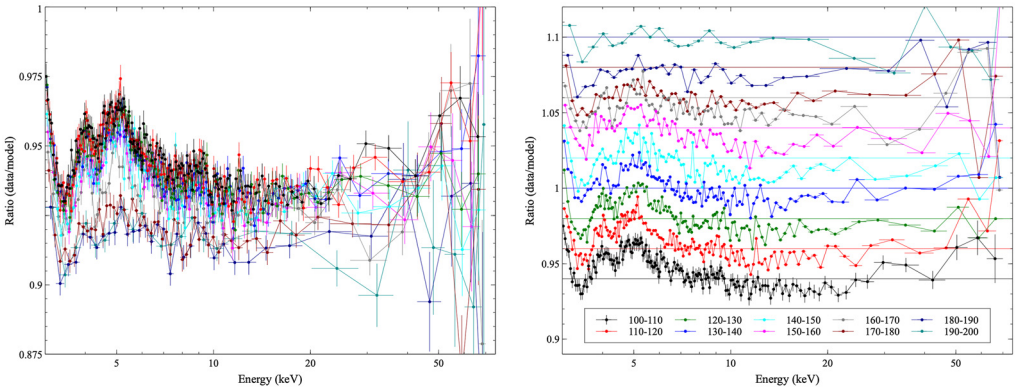

Fig. 5 FPMA ratio of the data to the Crab model for off-axis bins 100 to 200″. (a) The curves maintained at their absolute value. (b) The curves have been offset by 0.02, as indicated by the straight horizontal line for the same color and error bars removed for clarity. Systematic variations from bin to bin are evident.

index to be $\Gamma = 2.1 \pm 0.03$ and $N = 9.7 \pm 1.0$ keV^{-1} cm^{-2} s^{-1} at 1 keV. In Madsen et al's work,[7] we measured the Crab spectrum using the SL observations to a much higher precision of $\Gamma = 2.106 \pm 0.006$ and $N = 9.71 \pm 0.16$. Applying the same method, but with a lot more data, we refine this measurement in this paper to $\Gamma = 2.103 \pm 0.001$ and $N = 9.69 \pm 0.02$ as will be discussed in Sec. 5.2.2.

For the galactic absorption, N_H, we use tbabs with Wilms et al.'s[18] abundances and Verner et al.'s[19] cross-sections. The N_H of the Crab has over the years taken on a range of values as measured by different observatories, but it is mostly constrained between 2×10^{21} cm^{-2} and 6×10^{21} cm^{-2}, with an average value of $\sim 4 \times 10^{21}$ cm^{-2}.[6] In the original NuSTAR calibration in 2013, we measured the Crab column to be $N_H = 2.2 \pm 2.0 \times 10^{21}$ cm^{-2}.[4] Since this component will be degenerate with some of the instrument components, we decided to maintain this value, and in everything that follows the N_H will be frozen at $N_H = 2.2 \pm 2.0 \times 10^{21}$ cm^{-2}.

Figure 6 shows a range of N_H and the impact it would have if it were different than presumed. At the NuSTAR lower calibration boundary of 3 keV, this could potentially account for a 1% to 2% error, which will be transferred into the instrument response. This translates into a systematic

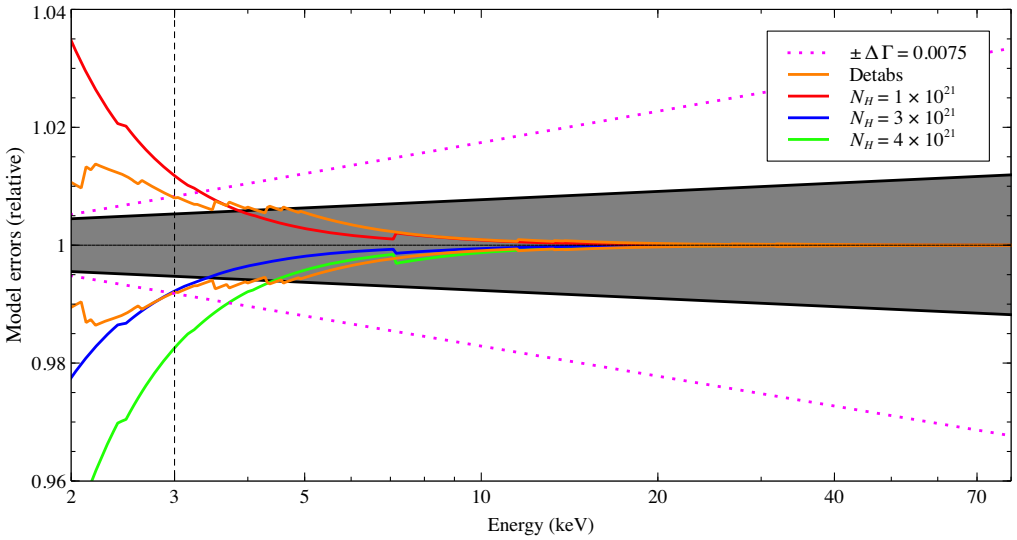

Fig. 6 Ratio of alternate models to the Crab model of $\Gamma = 2.1$ and $N_H = 2.2$. Shaded gray area is the fit obtained in Sec. 5.2.2 bounded by the 1σ errors. The DETABS curves are 1σ deviations to the parameters for Det0A in Table 3.

uncertainty on N_H that will be on the order of the measured range of N_H in Crab. The typical statistical errors in fitting N_H down to 3 keV in NuSTAR are of the order $\sim 1 \times 10^{21}$ cm^{-2}.

5 Detector Absorption and RMF Calibration

Below 5 keV, the instrument response is composed of several partially degenerate absorption effects as shown in Fig. 7. Starting from the sky-side, the photon first encounters a layer of MLI before entering the optics and exiting again through another layer of MLI. The complications and challenges of calibrating the MLI are discussed in Madsen et al.'s work,[8] but to summarize: the thickness of the MLI layer was absolutely calibrated on the ground pre-launch, and in-orbit re-calibration is only possible on relative differences, which we performed for FPMA after discovering that one of the layers had ripped. When the photon reaches the focal plane bench, it enters the FPMs through a Be window, which like the MLI was calibrated on the ground. We have not performed a re-calibration of this window, and do not intend to, as the only change to this calibration is if it gets punctured by a micrometeorite of which there is no evidence. At the detector surface, a Pt contact coating and an inactive CdZnTe dead layer cause absorption before the photon interacts in the active region of the detector. Unlike the MLI and Be window, no ground calibration of the dead layer was performed. The thickness of these layers, collectively referred to as DETABS, is measured in-orbit under the assumption that the MLI and Be thicknesses are constant. Finally, the detectors lose some quantum efficiency across the same energies due to electronic and charge transport effects.

These components are degenerate because all of them have a similar effect on the spectrum. During the previous calibration, the DETABS and the detector efficiency became partially entangled with the vignetting function; the correction to the vignetting was used to collectively correct inaccuracies across all sub-components that, at the time, had insufficient data to be corrected individually. After nearly 10 years in orbit, we now have the capability to perform this task.

In this section, we use Crab SL observations,[7,17] which are observations where the source flux bypasses the optics and falls directly on the detectors, to remove the degeneracy from the vignetting function. NuSTAR has a legacy program monitoring the Crab in the SL configuration. We use this data from several epochs to measure the thickness of the Pt and CdZnTe layers between 3 and 40 keV. Once we have those values we can the adjust the RMF between 2.2 and 5 keV. The valid lower energy bound of NuSTAR remains at 3 keV, but we calibrate down to 2.2 keV to ensure that the detector redistribution within the RMF does not cause problems at 3 keV. The Crab spectrum itself is fitted at the same time and gives us an absolute Crab flux reference. The time-averaged Crab spectrum over all epochs obtained from this data set is then used in the subsequent vignetting correction as the absolute reference.

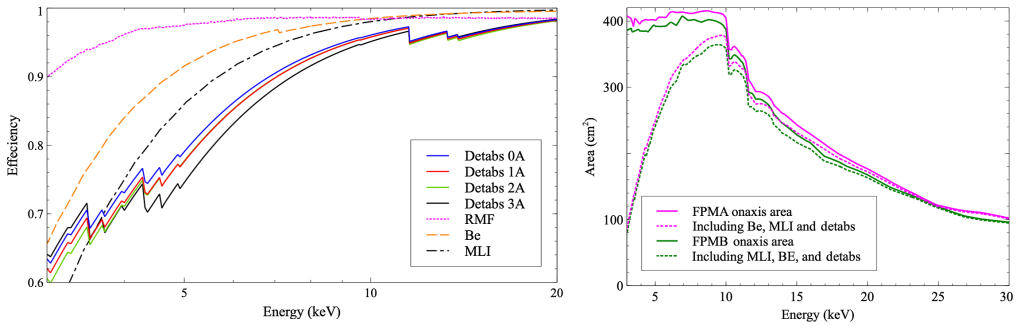

Fig. 7 (a) Low-energy absorption components for FPMA. Values for FPMA DETABS given in Table 3. (b) Effective area curves of FPMA and FPMB with and without the Be, MLI, and Detabs (for DetO). RMF quantum efficiency is not included.

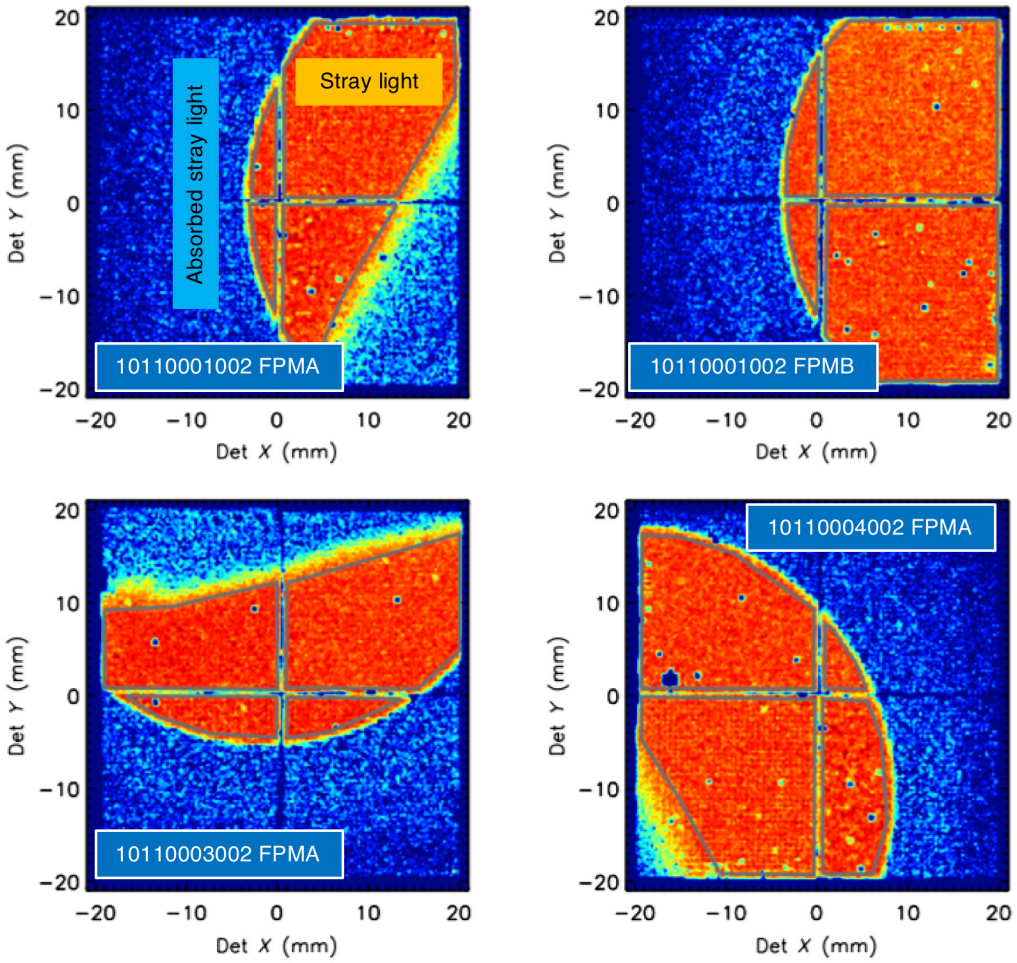

Fig. 8 Contour color plots of the detectors with logarithmic scaling. Green polygons show extraction regions, which are done for each detector individually. Due to the partially absorbed SL, backgrounds can not be taken from the same observation where there is SL.

5.1 *Observations and Data Reductions*

SL observations are performed by placing the source at ∼1 deg off-axis, which maximises the amount of SL and roughly covers half the field-of-view (FOV). If the source is moved closer, it gets blocked by the optical bench and further away less SL falls on the detector. Figure 8 shows examples of SL from the Crab, some of which are starting to be blocked by the optical bench. Due to the geometry of the observatory, at most two detectors can be covered at a time. The circular shape comes from the cutout in the aperture stops. In addition to the regular SL there is a partially absorbed SL component as well (see Fig. 8, top left). This is hard source flux being transmitted through the solid part of the aperture stops.[17] Since this is always present in the area adjacent to the main SL it precludes taking a background from the same observation.

For this reason, the legacy Crab SL observations are accompanied by blank-sky background observations taken at ∼10 deg from the Crab at a RA = 75 deg and DEC = 13 deg. This area is outside the absorbed stray light cone of the Crab and there are no other bright and hard x-ray sources within 10 deg that may result in an additional background component. Changes in the Galactic Ridge x-ray emission due to the different background position is not an issue at these energies. For more information on the NuSTAR background components, we refer to Refs. 20 and 21. Table 2 gives all the SL observations used here with their background observations.

The SL data are reduced with nupipeline, distributed with NUSTARDAS, using default settings and the background filters set to the appropriate parameters as evaluated from the background filtering diagnostic pages.[22] We do not use *nuproducts* for spectral extraction,

Table 2 Stray light observing log.

Epoch	Obsid	Bkg Obsid	Exposure time (s)	Module list[a]	Detector list[b]
October 2015	10110001002	10110002002	18961	A,A,A,A	0,1,2,3
October 2015	10110001002	10110004002	18961	B,B,B,B	0,1,2,3
October 2015	10110003002	10110004002	19299	B,B	0,1
April 2016	10110004002	10110005001	20888	A,A,A	1,2,3
April 2016	10110005001	10110004002	21776	B,B	0,1
February 2017	10210001002	10210002002	20173	A,A,B,B	0,3,0,3
April 1017	10210001003	10210002003	18158	A,A,B,B	0,3,0,3
July 2017	10311001002	10311002004	17305	A,A,B,B	0,3,0,3
September 2017	10311001004	10311002004	17911	A,A,B,B	0,3,0,3
October 2017	10311001006	10311002006	20442	A,A,B,B	0,3,0,3
November 2017	10311001008	10311002008	19467	A,A,B,B	0,3,0,3
March 2018	10402002002	10402006002	19133	A,A,B,B	0,3,0,3
March 2018	10402002004	10402006002	20848	A,A,B,B	0,3,0,3
March 2018	10402002006	10402006002	20085	A,A,B,B	0,3,0,3
May 2018	10402008002	10502004002	13877	A,A,B,B	0,3,0,3
September 2018	10402002002	10402003002	19280	A,A,B,B	0,3,0,3
September 2018	10402002004	10402003002	20848	A,A,B,B	0,3,0,3
September 2018	10402002006	10402003002	20085	A,A,B,B	0,3,0,3
February 2019	10502002002	10502004002	28704	A,A,B,B	0,3,0,3
March 2019	10502002004	10502004002	28705	A,A,B,B	0,3,0,3
May 2019a	10502006002	10502009001	31675	A,A	1,2
May 2019b	10502007002	10502009001	32072	B,B	0,1
August 2019a	10502010001	10502009001	19038	A,A,B,B	0,3,0,3
August 2019b	10502010003	10502009003	20357	A,A,B,B	0,3,0,3
February 2020	10602003002	10602004002	32410	A,A,B,B	0,3,0,3
February 2020	10602003004	10602004002	14760	A,A,B,B	0,3,0,3
August 2020	10602005002	10602004005	14248	A,A,B,B	0,3,0,3
August 2020	10602005004	10602004005	24338	A,A,B,B	0,3,0,3
February 2021	10702305002	10702004002	23410	A,A,B,B	0,3,0,3
Total	—	—	527529	—	—

[a]List of modules where stray light is taken.
[b]List of detectors to go with module list where stray light is taken.

but created custom tools to extract the data in detector coordinates.[7] These tools have since been ported into Python for general use and are described in more detail in Grefenstette et al.[23] Here, however, we use the original tools, which allow for greater flexibility and adjustment. In short, the procedure creates an ARF, which is the geometric area illuminated by the source on the detector, adjusted by the dead pixel area, and absorped by Be from the FPM entrance window. As shown in Fig. 8, the SL spectra are extracted detector-by-detector since the DETABS parameters are distinct to the individual detectors and are the values we want to recover. Since the spectra are only taken from individual detectors we can directly use the intermediate RMF v3.0 described in Sec. 5.2.3 without needing to generate a detector weighted RMF.

5.2 *Stray-Light Analysis*

The SL analysis is divided into two sections: (1) the DETABS measurement, DETABS, and (2) the RMF correction. The two effects are partially coupled but can be separated by first evaluating the DETABS. As shown in Fig. 7, the DETABS affects the spectrum most severely and persists all the way up to 40 keV, whereas the loss in efficiency in the spectrum due to the RMF is a much shallower function that remains approximately constant above 5 keV (∼98%). Above 5 keV, the detector response is well understood, but due to incorrect levels of electronic noise and pixel thresholds in the simulator used to produce the RMF there are issues below 5 keV. Since the DETABS is the dominant component, we can get a good estimate on the DETABS parameters even with an RMF that has low-energy issues as discussed in Sec. 5.2.3. The residuals that remain after the DETABS fitting has been performed we attribute to the RMF.

5.2.1 *Detector absorption*

We built an XSPEC absorption model, nuabs, with cross-sections for Pt and CdZnTe created by Geant4, with the adopted photon interaction model coming from the Livermore low-energy EM model based on the evaluated photon data library, EPDL97.[24] We multiply nuabs onto the Crab model (nuabs × tbabs × pow) and fit for the Pt and CdZnTe thickness. The fit is performed using 110 data sets (there are on average four data sets per observation; 2 for FPMA and 2 for FPMB). We tie together the Pt and CdZnTe parameters for the same detector across all epochs but allow the Crab spectrum to vary from epoch to epoch, only tying together the Crab parameters across detectors within the same epoch.

We simultaneously fitted eight detector Pt and CdZnTe parameter pairs over 20 Crab epochs and experimented with the fitting range to ensure the stability of the fit. We are confident about the 5- to 20-keV energy band, which is above where the RMF has issues and below where the background begins to affect the spectrum. The stability of the fit, however, was not good and the DETABS parameters took on unlikely values, which meant there were degeneracies between the Crab spectrum and DETABS. Expanding this down to 3 keV improved the stability, but the Crab spectral parameters had to be managed in order not to rail at extreme values, which again caused the DETABS parameters to take on unrealistic values. Expanding the energy range up to 40 keV solved the stability issues due to the long lever arm on the Crab spectrum and the restriction that had on allowed values DETABS can take. Figure 9 shows the changes in the DETABS absorption in the 3 to 20 keV and 5 to 20 keV range with respect to 3 to 40 keV, and the large absorption troughs generated by the narrower fitting bands, due to very a large Pt thickness, were not feasible.

The key parameters for DETABS v004 to the 3- to 40-keV fit are summarized in Table 3, and Fig. 10 shows the remaining residuals for FPMA and FPMB, Det0 and Det3, for all observations at 2 to 4 keV after the fit. The residuals are independent of epoch and distinct for each detector, which confirms that the remaining issues are tied exclusively to the detector response.

5.2.2 *Epoch averaged Crab SL spectrum*

When computing the corrections to the RMF (Sec. 5.2.3) and the vignetting function, (Sec. 6) we need to first produce a canonical Crab model to calibrate against. Ideally, we would want to do this epoch-by-epoch with SL observations matched to every focused observation.

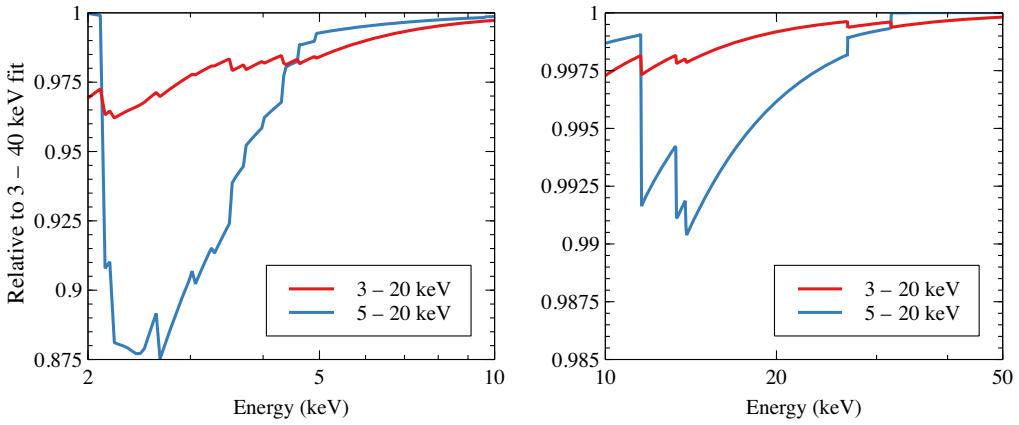

Fig. 9 DETABS component for Det0A for different fit energy constraints and energy bands relative to the 3- to 40-keV fit.

Table 3 DETABS v004 parameters.

Module	Detector	Pt (μm)	1σ	CdZnTe (μm)	1σ
A	0	0.090	0.001	0.245	0.008
A	1	0.093	0.004	0.276	0.026
A	2	0.072	0.005	0.419	0.030
A	3	0.100	0.001	0.250	0.008
B	0	0.101	0.001	0.235	0.008
B	1	0.080	0.003	0.274	0.020
B	2	0.081	0.012	0.284	0.070
B	3	0.084	0.001	0.225	0.008

We unfortunately do not have matched SL and focused observations (Tables 2 and 6) for all epochs. In addition, the new calibration method described in Sec. 3.1.1 mixes together different epochs of the focused observations to produce meta spectra binned by off-axis angle. Finally, to produce enough signal-to-noise to reduce the statistical errors to the $\sim$2%, we have to combine all of the SL data for each detector, thereby also mixing epochs.

We include the variations in the Crab spectrum itself as a source of systematic noise, and we can evaluate the approximate magnitude of this systematic error by looking at variations within the NuSTAR data and comparing this to monitoring observatories such as Swift/ Burst Alert Telescope (BAT), which will be done in Sec. 7. Here, we assume that both the RMF and the Crab are stable in time.

To produce the canonical model, we fit the SL data from all epochs over the energy range between 5 and 20 keV. In this range, the responses are best known and minimally impacted by the low-energy RMF issues (yet to be calibrated out) and background inaccuracies. We performed this epoch-average fit in two ways: (1) fitting all of the 110 SL data sets simultaneously to the same Crab model, and (2) first combining all data and background into detector-specific spectra, which are then fit to the same Crab model. We load the DETABS v004 parameters from Table 3 and keep them frozen in the nuabs model. The results from the two methods are shown in Table 4, and they are consistent within errors, so we adopt the average of these two results, $\Gamma = 2.103 \pm 0.001$ and $N = 9.69 \pm 0.02$ keV^{-1} cm^{-2} s^{-1} at 1 keV, and hereafter, define to the canonical Crab model to be $\Gamma \equiv 2.103$ and $N \equiv 9.69$.

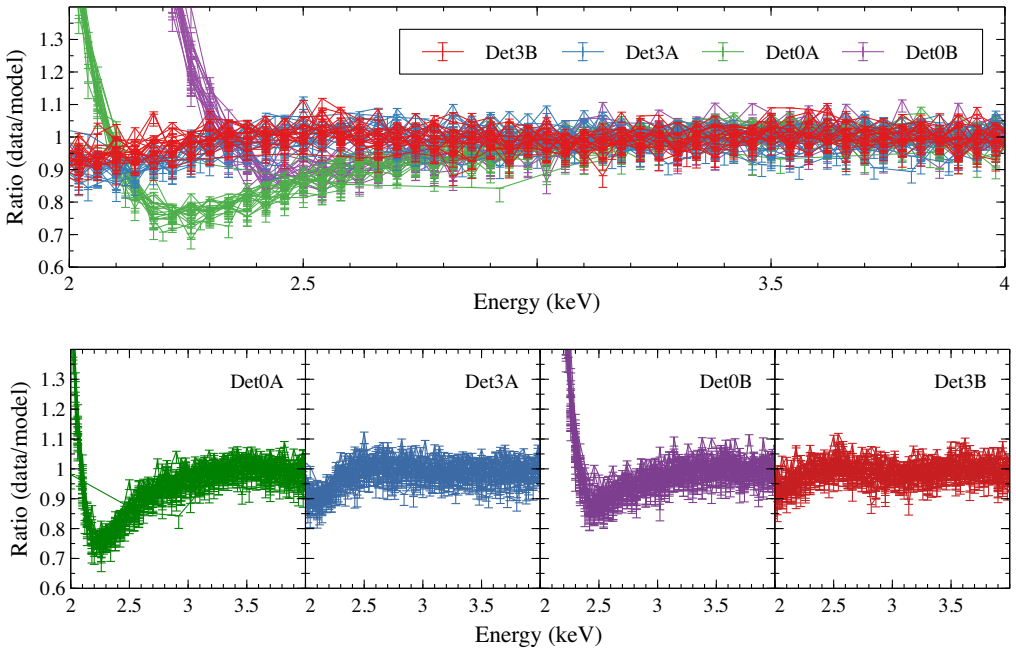

Fig. 10 Ratio of the SL data to the canonical Crab spectrum summarized in Table 4 for FPMA and FPMB, Det0 and Det3, after determination of the nuabs parameters. These remaining residuals are attributed to the RMF.

5.2.3 *RMF calibration*

The readout architecture for the NuSTAR detectors directly measures the charge collected by each pixel. The resulting signal is sent to a "fast" trigger chain, which has a shaping time of a few μs. If the signal exceeds the trigger criteria, then the event is read out. The two main parameters involved in the readout of the fast chain are: the trigger threshold itself (μ) and the noise on the shaping amplifier (σ).[25] The trigger thresholds are typically set to be $\sim$2 keV, though this is a software-programmable value that changes the average threshold for each detector, and pixel-to-pixel component variations can lead to effective "gain" differences on the fast chain that affect the apparent value of μ. σ may also vary detector-by-detector.

In our comparison of the Crab model with the RMF, we found that Det0 on FPMA and FPMB are both close to the nominal 2-keV threshold. However, for the other three detectors we measure a lower threshold. In fact, for FPMB Det1 and Det3, the threshold is actually below the nominal "PI channel 0." This is due to an artificial floor in the definition of the NuSTAR PI channel scale, which starts at 1.6 keV. In principle, this means that we could adjust the definition of the PI channels down to enable more low-energy analysis of the NuSTAR data. However, this is beyond the scope of the current calibration effort as it would likely result in substantial confusion in the community.

In addition to the differences in the threshold value, we also noted that the measured drop off in quantum efficiency was markedly broader than what was captured in the simulated RMFs. This can be explained by an unmodeled source of noise in the fast electronics chain that was not accounted for (e.g., the value of σ was incorrect). We note that this noise term is completely unrelated to any energy resolution effects and only affects the shape of the quantum efficiency curve at low energies.

In the previous version of the GEANT4 code that generated the RMF, the threshold values for all pixels was assumed to have a single value (2 keV) and the σ term was assumed to be negligible. This resulted in an overly "sharp" cutoff in the RMF at 2 keV. Because a large fraction of the events in NuSTAR result from sharing charge between neighboring pixels, the impact of improperly calibrating the RMF threshold could become apparent at roughly 2$\times$ the trigger level (so, 4 keV).

Table 4 Crab spectral parameters. Fit 5 to 20 keV.

Epoch	Γ	Normalization	Flux (3–10 keV) (10^{-8} ergs cm^{-2} s^{-1})
October 2015	2.091 ± 0.010	9.32 ± 0.06	1.540 ± 0.010
April 2016	2.109 ± 0.009	9.73 ± 0.08	1.560 ± 0.012
February 2017	2.105 ± 0.010	9.61 ± 0.06	1.552 ± 0.010
April 2017	2.101 ± 0.010	9.60 ± 0.03	1.561 ± 0.005
July 2017	2.103 ± 0.010	9.63 ± 0.07	1.561 ± 0.011
September 2017	2.101 ± 0.010	9.59 ± 0.03	1.558 ± 0.005
September 2017	2.097 ± 0.005	9.47 ± 0.06	1.549 ± 0.010
October 2017	2.102 ± 0.010	9.53 ± 0.06	1.548 ± 0.010
November 2017	2.101 ± 0.005	9.65 ± 0.05	1.569 ± 0.008
March 2018	2.101 ± 0.011	9.62 ± 0.08	1.562 ± 0.012
May 2018	2.101 ± 0.007	9.63 ± 0.05	1.566 ± 0.008
September 2018	2.099 ± 0.009	9.49 ± 0.06	1.548 ± 0.009
February 2018	2.107 ± 0.009	9.61 ± 0.03	1.545 ± 0.005
March 2019	2.102 ± 0.020	9.52 ± 0.13	1.546 ± 0.021
May 2019a	2.105 ± 0.012	9.65 ± 0.08	1.558 ± 0.013
May 2019b	2.092 ± 0.010	9.39 ± 0.06	1.548 ± 0.010
August 2019a	2.099 ± 0.009	9.49 ± 0.06	1.549 ± 0.010
August 2019b	2.101 ± 0.006	9.64 ± 0.05	1.567 ± 0.008
February 2020	2.107 ± 0.006	9.76 ± 0.06	1.571 ± 0.009
August 2020	2.098 ± 0.007	9.55 ± 0.03	1.560 ± 0.005
Epoch average[a]	2.103 ± 0.002	9.65 ± 0.01	1.56 ± 0.002
Epoch average[b]	2.103 ± 0.002	9.73 ± 0.01	1.57 ± 0.002
Canonical	2.103 ± 0.002	9.69 ± 0.01	1.57 ± 0.002

[a]Simultaneous fit to all 110 SL data sets.
[b]Simultaneous fit to detector combined data.

We updated the RMF code to properly account for the coarse measurements of μ and σ made using the nearest neighbor analysis method.[25] For all detectors, the noise term was consistent with 0.7 keV, whereas the updated μ values are shown in Table 5. In addition to adjusting the threshold, we also increased the number of incident photons from 1.44 to 14.4 M to reduce the impact of numerical statistical fluctuations in the quantum efficiency (QE) curve to roughly 0.35%. A comparison of the 2010v002 RMFs and the updated RMFs v3.0 from the GEANT4 simulation are shown in Fig. 11.

The SL data were reduced using this intermediate RMF v3.0, and to correct the features seen in Fig. 10 (such as the distinctive "swoop" seen in Det0), we applied a correction function on the RMF v3.0 input channel. This effectively means the correction is redistributed in energy and the output efficiency is a superposition of corrections from several channels. Figure 12 shows an example fit for Det0A and illustrates that the corrected RMF v3.1 has more structured variations at the 2 to 4 keV turnover than the simulated RMF v3.0.

Table 5 RMF threshold parameters.

Module	Detector	μ (keV)
A	0	2.0
A	1	1.83
A	2	1.88
A	3	1.7
B	0	2.1
B	1	1.42
B	2	1.68
B	3	1.45

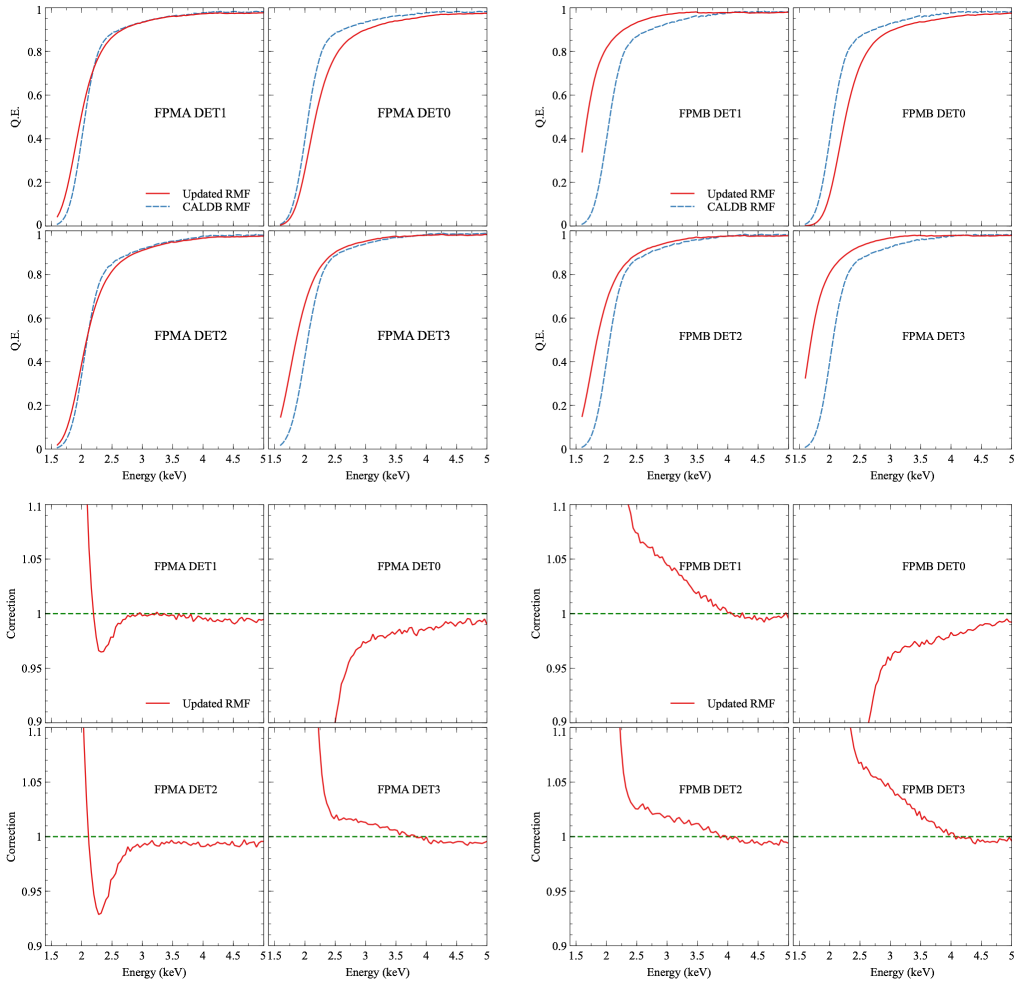

Fig. 11 Top panel: comparison of the simulated quantum efficiency in FPMA (left) and FPMB (right) for the CALDB RMFs (blue, dashed) compared with the v3.0 RMFs with the corrected μ and σ values (red, solid). Bottom panel: the difference in quantum efficiency between the CALDB RMFs and the v3.0 RMFs. This is before application of the Crab correction.

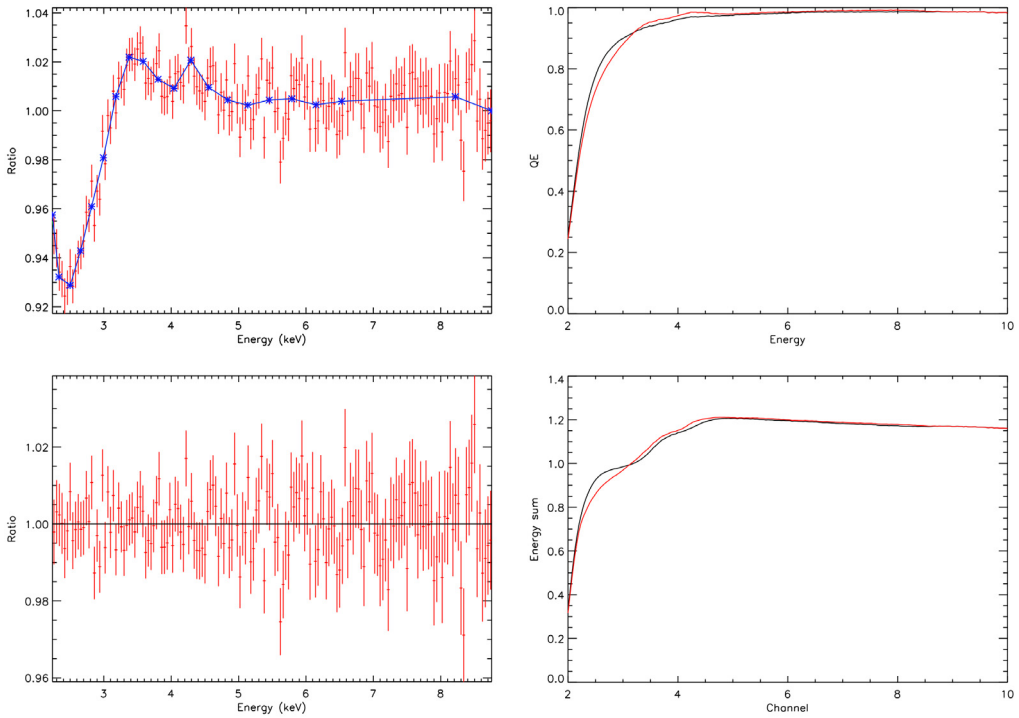

Fig. 12 Top left: ratio of the canonical model before correction, over plotted (in blue) with the correction folded through the response (v3.0) and where stars denote the grid points of the fit for Det0A. Bottom left: ratio of canonical model after application of the corrected RMF (v3.1). Right top: RMF v3.0 (black) and RMF v3.1 (red) summed along the channel axis. Right bottom: RMF v3.0 (black) and RMF v3.1 (red) summed along the energy axis.

6 Effective Area Calibration

6.1 *Observations and Data Reductions*

The on-going NuSTAR Crab calibration campaign measures the Crab spectrum at various off-axis angles. This has to date resulted in 71 individual observations listed in Table 6 with a total single FPM exposure time of 233 ks. Figure 2 (right) shows the distribution of all counts within the 3- to 78-keV band as a function of off-axis angle for FPMA and FPMB. The counts peak at $\sim 1.5'$, which is the default NuSTAR "on-axis" position (moving closer to the optical axis causes the source to fall into detector gaps), and overall there is more than 10^6 counts per off-axis bin up to $7'$.

In the data reduction, we treat the Crab as a point source despite its angular extent ($\sim 120'' \times 100''$) since the center of the nebula where the pulsar resides dominates the emission. The difference in the effective area response between a point source extraction centered on the pulsar and an extended source extraction is only $\sim 1\%$ to 2%, and therefore, an acceptable error. But, most importantly, by treating the Crab as a point source it allows us to use the built-in pipeline corrections for the aperture stop, ghost ray, and PSF corrections (for details on these components see Madsen et al.[4,7,17]). These corrections are not applicable to extended source responses; since certain off-axis angels can be larger than the error introduced by assuming the Crab is a point source, they are important to include. We extract counts from a $200''$ region, which includes $\sim 95\%$ of all photons in the source extraction region. The 95% are corrected for in the PSF.

We run nupipeline with default settings but include the statusexpr keyword (STATUS == b0000xx000 xxxx000), which allows good events rejected due to high countrates to be included. In addition to default settings we also applied the temperature dependent MLI correction for the identified subset marked in Table 6, and we excluded observations if the pulsar of the Crab fell into a detector gap. Since much of the flux comes from the pulsar, which has a significantly

Table 6 Focused CCrab observing log.

Obsid	Mean off-axis angle (arcmin)	Exposure time (s)	Obsid	Mean off-axis angle (arcmin)	Exposure time (s)
10013021002	3.6	2275	10013022002	1.5	2592
10013022004	1.5	2347	10013022006	1.4	2587
10013023002	4.1	2102	10013024002	4.7	2258
10013025002	5.0	1235	10013025004	5.0	1161
10013025006	4.8	1593	10013026002	5.5	2540
10013026004	5.7	1162	10013027002	5.8	1182
10013027004	5.6	1105	10013028002	6.5	1601
10013028004	6.7	1254	10013029001	4.4	2909
10013030001	4.4	3023	10013031002	1.9	2507
10013032002	1.3	2595	10013033002[a]	1.5	1383
10013033004[b]	1.3	1269	10013034002	1.2	988
10013034004[c]	0.8	5720	10013034005[c]	0.9	5968
10013035002	5.4	9401	10013036002	5.8	179
10013037002	2.0	2679	10013037004	2.9	2796
10013037006	2.9	2799	10013037008	3.1	2814
10013038002	3.9	3084	10013038004	3.9	2217
10013038006	4.0	266	10013038008	4.0	2231
10013039002	4.1	590	10013039003	4.2	583
80001022002	1.5	3917	10002001002	1.6	2608
10002001004	1.6	2386	10002001006	1.4	14263
10002001008	1.6	4941	10002001009	1.3	5198
10202001002[a]	1.1	1454	10202001004	2.0	9025
10202001006	1.7	4307	10202001007	2.9	4104
10302001002	2.5	4300	10302001004	1.2	7547
10302001006[a]	1.0	3729	10402001002[a]	1.1	9436
10402001004	1.4	3312	10402001006	1.4	4757
10402001008	1.3	5657	10402001010	1.9	1133
10402001012	1.8	1270	10402001014	1.8	1284
10402001016	1.8	1169	10502001002	2.8	2676
10502001004	2.3	2022	10502001006[d]	2.2	3949
10502001008[d]	1.9	2417	10502001010	2.1	432
10502001011	4.0	9553	10502001013	2.0	7665
10502001015	2.3	7492	10602002002	2.2	3567

Table 6 (*Continued*).

Obsid	Mean off-axis angle (arcmin)	Exposure time (s)	Obsid	Mean off-axis angle (arcmin)	Exposure time (s)
10602002004	2.1	3590	10602002006	1.9	2209
10602002008	2.0	2514	10702303002	1.9	2957
10702303004	2.0	3150	—	—	—
Total	233020 s	—	—	—	—

[a]Not used for either but included in tests.
[b]Not included for FPMA.
[c]Not included for FPMB.
[d]MLI temperature correction.

harder spectrum than the PWN,[26] both simulations and observations show that loss of this component will distort the spectrum and make it unsuitable for calibration. After the pipeline has run, we find the good time intervals (GTI) that subdivides each observation into the respective off-axis angle bins. The source off-axis angle is the angular distance between the optical axis and the source center. We calculate the off-axis angle as a function of time from the _det1.fits file produced by nupipeline, which defines for each time bin where the optical axis was in coordinates of the sky. The generated GTI files are input into nuproducts to split the observations into the angle specific spectra. We combine the GTI sorted spectra and their backgrounds into the final off-axis angle bin using the FTOOL addascaspec and combine the RMF using addrmf.

6.1.1 *Background*

Obtaining backgrounds for the Crab observations presented us with some challenges. Background starts to affect the spectrum at the 1% level at ∼55 keV, which at these energies is mostly internal detector background.[20] However, because of the Crab's brightness and the extent of the PSF, we can not extract a local background from the same observation. Along with the SL observations mentioned above, we take blank backgrounds a few degrees from the Crab. There are multiple observations, and we combine the best of them into a master background. Since the Crab is either observed at sky position angle (roll of the FOV) of PA = 150 deg or PA = 330 deg, we combine the backgrounds separately for the two PA, which allows us to use the NUSTARDAS extraction pipeline to directly apply the extraction region from the source image to the background.

The projection of the detector on the sky is never the same for any observation, and we have to remove the spacecraft jitter from the background observations as well before stacking them. This is a non-standard procedure that involves correcting files that track the center of the detector on the sky to produce a jitter-free image. In this manner, we combine together several jitter-corrected background observations listed in Table 7 into two master backgrounds with over 100 ks exposure. Figure 13 shows the background spectrum from the master backgrounds, and at low energies FPMA has a slightly lower background due to the background variations produced by the shadow of the optical bench as described in Ref. 20. There is no difference between the backgrounds at the two PA positions, and the splitting into PA purely one related to compatibility with the pipeline software.

By definition, when filtering on off-axis angle, the source position on the detector is stable and virtually jitter-free (since the spacecraft/mast jitter is what causes the off-axis angle variations), and we can therefore extract the background from the same location on the detector where the source falls, ensuring that we are sampling the correct instrumental background.

We make a note here that the background treatment is the only step in the data preparation that does not involve the regular NUSTARDAS and FTOOLS. Less precise background can be obtained by extracting from individual background fields closest in time to the observation as was done for the SL analysis.

Table 7 Backgrounds for focused observations.

Obsid For PA = 150 deg	Exposure time (s)	Obsid For PA = 330 deg	Expsoure time (s)
10311002002	16048	10210002002	20567
10311002006	14898	10402006002	17427
10311002008	18633	10502004002	14418
10402005002	26826	10502004004	15210
10602004005	28207	10602004002	47886
—	—	10602004003	38184
—	—	10702004002	39740
Total	104612	Total	193432

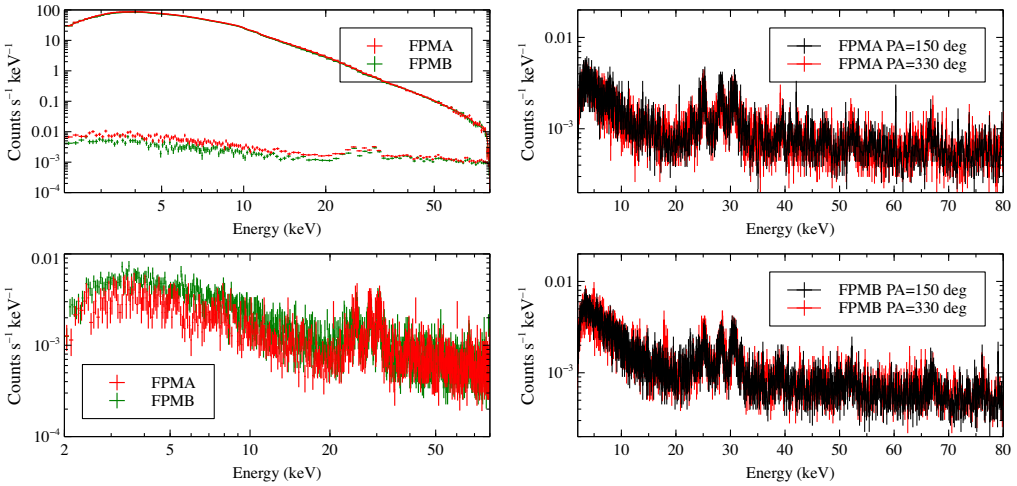

Fig. 13 Top left: example spectrum and background extracted from a circle with a radius of 200″ for Crab observation 10002002002. Bottom left: backgrounds extract from 160″ on Det0 for the master background at PA = 150 deg. Right panel: Master backgrounds extracted from Det0 for PA = 150 deg and PA = 330 deg for FPMA and FPMB. There is no measurable difference between the two PA positions, and the splitting of the backgrounds purely one related to compatibility with NUSTARDAS.

6.2 *Fitting Procedure*

In Sec. 5.2.2, we found from the combined fit to all SL observations that $\Gamma = 2.103 \pm 0.001$ and $N = 9.69 \pm 0.02$ keV^{-1} cm^{-2} s^{-1} at 1 keV, which we will refer to as the canonical Crab model, $M_{\rm crab}$. In practical terms for a spectrum with fixed energy bins, we can obtain the instrument count spectrum for $M_{\rm crab}$ for a fixed off-axis angle, θ, by folding this model through the response functions

$$C(PI)_{\rm instrument} = {\rm RMF}(PI, E) \circledast [{\rm ARF}(E) \times {\rm Corr}(E) \times M_{\rm crab}(E)], \quad (4)$$

where ARF(E) contains all the effective area corrections discussed in Sec. 3.1 and shown in Eq (3), and Corr(E) is the correction function we wish to find, which we have here moved out of the ARF. We compare this count spectrum to the observed spectrum and use least squares fitting of a piece-wise linear function to find the array elements of Corr(E). We do this for all θ (from 0′ to 7′ in steps of 10″) to obtain Corr(θ, E).

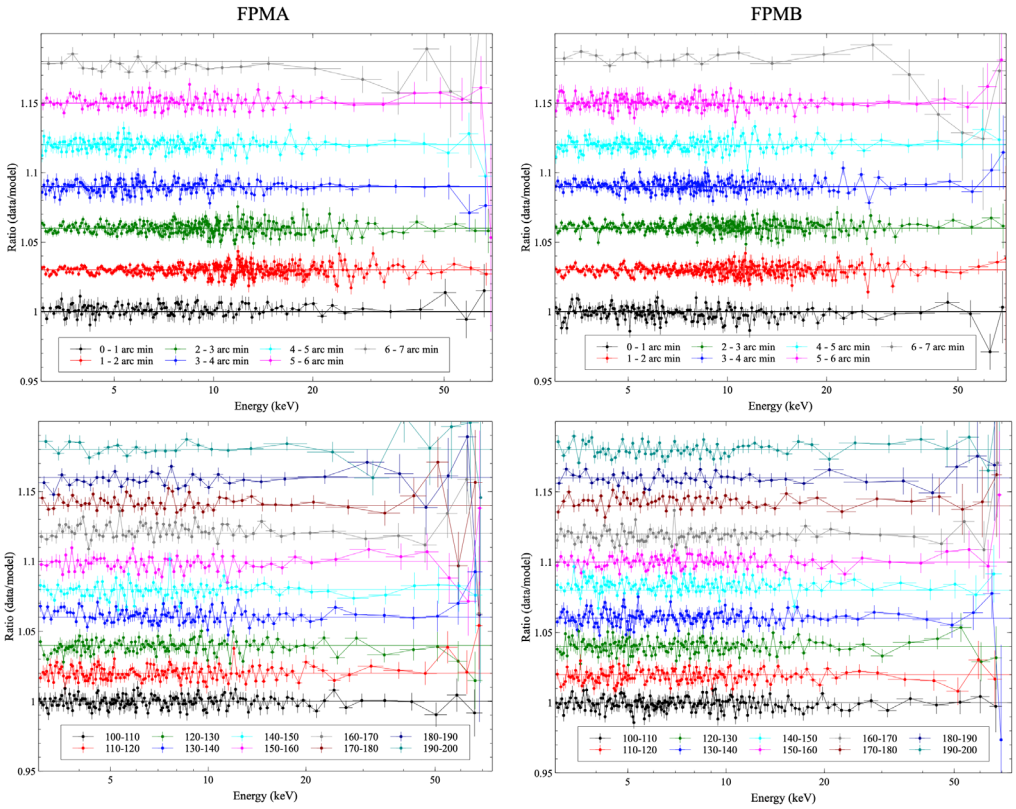

Fig. 14 Top panel: ratio plots for 60″, artificially offset for clarity. Separation between curves are 0.03 and indicated by the colored horizontal lines. Bottom panel: ratio plots for 10″ bins between 100″ to 200″. Separation between curves are 0.02 and indicated by the colored horizontal lines. These plots can be compared to Figs. 4 and 5.

This forward folding approach is necessary because the RMF is a non-diagonal matrix and cannot be inverted. This also means that the solution to $\mathrm{Corr}(E,\theta)$ is not necessarily unique and care must be taken to avoid non-physical solutions. This may occur when the RMF, due to energy redistribution, compensates for a disproportionately deep sharp trough or high peak with with an opposite extreme. This issue may be mitigated by choosing sensible binning and sufficient statistics in the grid of fitting points, which was met by a logarithmic binning in energy that varies depending on the fidelity of the spectrum.

We fitted each 10″ from 0″ out to 420″. Because each off-axis bin has different fidelity, the process required supervision by adjusting the binning and ranges to ensure good results. Figure 14 shows the spectra after correction with respect to the canonical reference Crab spectrum for 60″ bins (top panel) and for 10″ bins (bottom panel) for off-angle bins 100 to 200″. The residuals are on the order of $\pm 2\%$ below 50 keV, whereas above 50 keV there are larger deviations. The Crab is a soft x-ray source, and despite its brightness, the signal at high energies is limited, in particular, for higher off-axis angles where 5% to 10% residuals had to be tolerated.

7 Results

7.1 *Crab Results*

To quantify and validate the new responses (DETABS v004, RMF v3.1, and ARF v008), we applied them to all of the focused Crab observations and compared the data to the old responses (DETABS v003, RMF 2010v002, and ARF v007). The data were reduced using NUSTARDAS with the same conditions and parameters as discussed in Sec. 6.1. We fit between 3 and 70 keV, using the same absorbed powerlaw as before but without nuabs, which is now applied to the

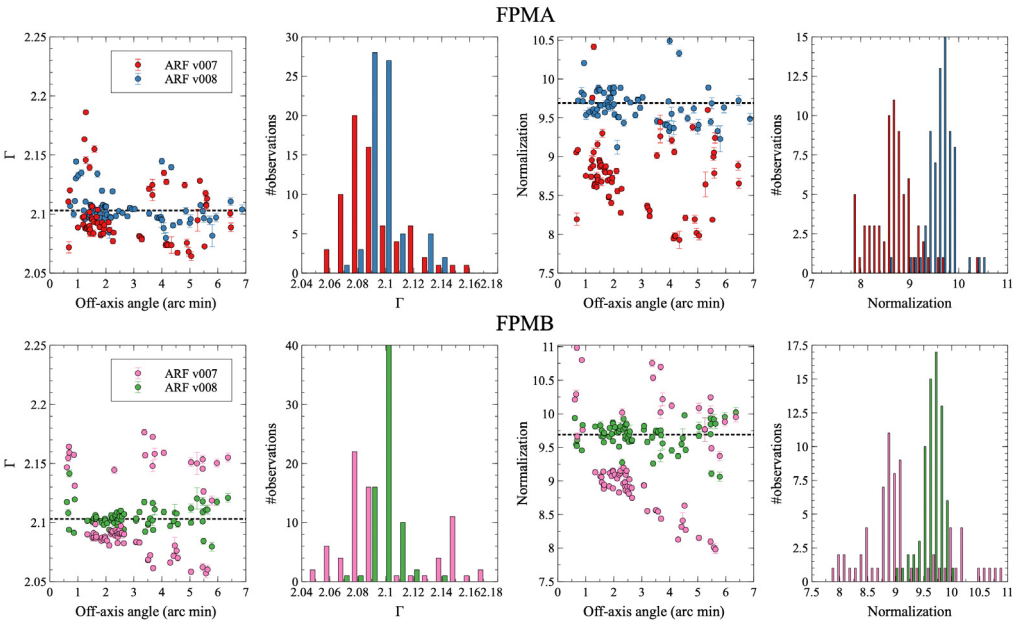

Fig. 15 Fitting results from all focused Crab observations from Table 6 were reduced with ARF v007 and v008. For the powerlaw slope, the spread in values is significantly improved above 3′ off-axis angle. Scatter still persists below 1′ due to the pulsar falling into the detector gaps, resulting in a change of the spectral parameters toward a softer value, and for FPMA there are two high points at 4′, which are due to the source straddling det2 and det3. For the normalization, we observe a clear trend as a function of off-axis angle for the old responses which has been corrected in the new responses. The resulting flux increase in reprocessed observations is therefore a function of the off-axis angle of the observation. The statistical average values are recorded in Table 8.

responses in NUSTARDAS. The results are shown in Fig. 15, and they demonstrate that we have succeeded in removing a strong dependency on off-axis angle in both slope and normalization that was present in the old responses. There still remains a minor residual slope at small and large off-axis angles, which are related to the source falling into the detector gaps at small off-axis angles, whereas for large off-axis angles there are complexities in the single-reflection component, which merges with the double-reflection PSF, along with the source being partially off the detector. Overall, though, for both modules the spread in slope and normalization has been significantly reduced in the new responses.

The question of how much of the residual structure is due to calibration and how much due to the intrinsic variations of the Crab still remains. To address this, we show in Fig. 16 a lightcurve in the 15- to 50-keV band from Swift/BAT with the fluxes of the NuSTAR focused and SL observations used here. The NuSTAR data have been normalized to the canonical flux between 3 to 10 keV, and the Swift/BAT data adjusted to be ∼1 at the beginning of the NuSTAR Crab observations. We also calculated the NuSTAR intensity in the 15- to 50-keV band directly from the countrates by subtracting the background and dividing with the response in each channel before summation, and it yielded exactly the same relative intensities as the fluxes derived from the model fit.

The long term Swift/BAT lightcurve shows a slow variation in the Crab that can be on the order of 1% to 2% per year, however, the NuSTAR data does not appear to be observing this trend toward late times when Swift/BAT is detecting a decrease. It is important to understand that although we have calibrated to a constant flux and slope, the re-calibrated responses do not have a time dependency. The only two time dependent components in NUSTARDAS is the gain, which is linear, and the MLI correction, which is step-wise.[8] Since neither of these components have been calibrated with respect to the Crab, there is no reason to suspect that they would counteract the observed Crab variations, and it remains unclear why the two observatories are not tracking the same variation. What we can say, is that the re-calibrated NuSTAR data varies less than what is observed with Swift/BAT.

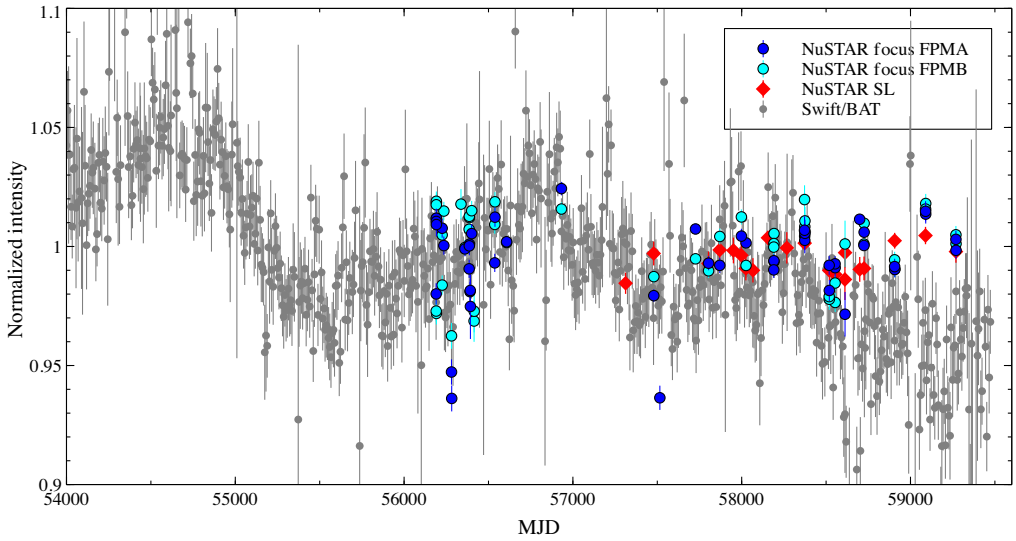

Fig. 16 Swift BAT 15- to 50-keV flux Crab lightcurve with NuSTAR SL and focused fluxes normalized to the 3- to 10-keV flux of the canonical Crab model used in this paper. The normalization between NuSTAR and Swift is relative and adjusted to be equal to 1 at the start of the NuSTAR Crab observations. For the NuSTAR focused data, we only show observations between 1 and 4′ off-axis.

Table 8 Mean and standard deviation of all focused Crab observations between 1′ to 4′.

Module	Γ	Normalization ($keV^{-1}\,cm^{-2}\,s^{-1}$)	Flux (3 to 10 keV) (10^{-8} ergs $cm^{-2}\,s^{-1}$)
ARF v007			
Crab[a]	2.1	8.5	1.38
FPMA	2.097 ± 0.023	8.74 ± 0.44	1.42 ± 0.033
FPMB	2.103 ± 0.033	9.20 ± 0.71	1.49 ± 0.042
ARF v008			
Crab[a]	2.103	9.69	1.57
FPMA	2.104 ± 0.013	9.66 ± 0.23	1.56 ± 0.026
FPMB	2.105 ± 0.009	9.68 ± 0.19	1.56 ± 0.028

[a]Canonical Crab values used for the calibration.

Since the remaining variations in the NuSTAR data do not appear to be driven by the Crab, we can consider the distribution of fluxes and slopes across epochs for the focused Crab observations to be a good upper limit of our systematic error for repeated measurements. Table 8 summarizes the mean and standard deviations of the slope (Γ), normalization, and the 3- to 10-keV flux for the focused observations with both the old and new responses. To avoid any bias from observations from low and high off-axis angles, we only evaluated the observations between 1′ and 4′. In conclusion, the systematic errors on the power-law slope is ± 0.01, which should be taken in conjunction with Fig. 6 that bounds the possible errors on the model components that might have been incurred due to our choice of $N_{\rm H}$. For the constraints on the flux, Figs. 16 and 17 should serve as a guide and $\pm 3\%$ taken as a conservative estimate.

Finally, we investigated the FPMA/FPMB ratio and show in Fig. 17 that with the new responses as a whole the distribution of ratios has been shifted and centered about 1. The spread,

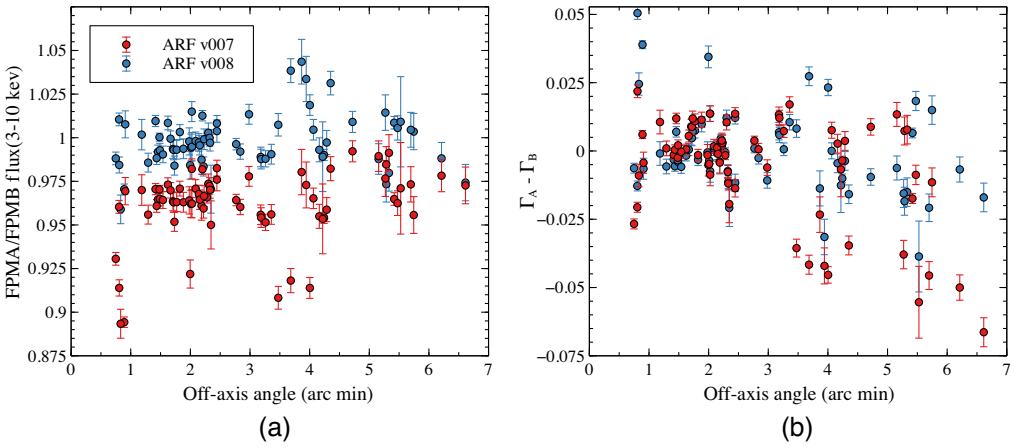

Fig. 17 (a) Flux ratio between FPMA and FPMB for 3 to 10 keV, demonstrating that overall the two modules are in better agreement with the new responses. The scatter is unchanged, which indicates it is driven by secondary geometrical corrections, such as the PSF corrections and detector gaps. (b) Delta of the powerlaw index between FPMA nd FPMB. Improvements can be seen for high off-axis angles.

however, largely remains the same, i.e., the difference between FPMA and FPMB with repeated observations has not significantly changed. We interpret this to mean that the remaining errors are driven by secondary geometrical corrections, such as detector gaps, PSF correction, dead pixels, and variations of DETABS and detector thresholds within the detector, which are out of scope of this work.

7.2 *Case Studies*

To further help clarify the changes, we present here a couple of case studies where we have applied the new CALDB to some published and public data spanning a range of brightness and source types. All of these source are at a typical location on the detector and without any technical challenges.

7.2.1 *TDE candidate SDSSJ143359.16+400636.0*

This observation of a tidel distuption event candidate took place on February 13, 2020 (Obdsid 90601606002) and published by Brightman et al.[27] The spectrum is quite soft ($\Gamma \sim 3$) and relatively faint (count rate ~0.1 cts/s). The original analysis was done jointly with 2 Chandra data sets and we included that data in the reanalysis too. The model used was a simple const × tbabs × powerlaw. Observed changes to these parameters were:

1. N_H: $(10^{20}\ \mathrm{cm}^{-2})$: $9.4 \pm 5.3 \rightarrow 8.1 \pm 5.3$
2. Γ: $2.90 \pm 0.11 \rightarrow 2.86 \pm 0.11$
3. norm: $1.16 \pm 0.20 \times 10^{-3} \rightarrow 1.15 \pm 0.20 \times 10^{-3}$
4. flux (erg cm^{-2} s^{-1}, 3–15 keV): $5.83 \pm 0.28 \times 10^{-13} \rightarrow 6.16 \pm 0.33 \times 10^{-12}$.

Most of the parameter changes are on the 1% to 2% level and much less than the uncertainties, with the exception of N_H, but as discussed the sensitivity to N_H in the NuSTAR band is $\sim 1 \times 10^{21}$ cm^{-2}. The change in flux is +5% as anticipated. This has no significant implications on the interpretation of the data.

7.2.2 *Ultra-compact x-ray binary 4U 1543-624*

Joint NuSTAR and NICER observations of the ultracompact x-ray binary (UCXB) 4U 1543-624 (Obsid 30601006002) were obtained in April 2020, and the data published by Ludlam et al.[28] The comparison was made for the NuSTAR data only, and just for the continuum modeling using

the model: constant × TBfeo × (bbody + cutoffpl). The refitted parameter values agree within the 90% confidence level, and the model flux (3 to 40 keV) are increased as shown by

1. FPMA: $3.6098 \times 10^{-10} \rightarrow 3.8952 \times 10^{-10}$ erg cm^{-2} s^{-1} (∼8% increase).
2. FPMB: $3.6511 \times 10^{-10} \rightarrow 3.8479 \times 10^{-10}$ erg cm^{-2} s^{-1} (∼5% increase).

The statistical errors are the same for the model flux before and after and not shown as they are not relevant to the flux increase estimation. Apart from the flux change there are no implications on the interpretation of the data.

7.2.3 *Black Hole X-ray Binary 4U 1543-475*

To evaluate the impact on more complex spectra, we investigated the bright black hole binary 4U 1543-475. This observation of 4U 1543-475 (obsid 90702326008) was a directors discretionary time (DDT) trigger performed on August 29, 2021. The source count rate in the 3- to 79-keV band was roughly 400 cts/s, resulting in about 3 million total counts per FPM. We show the ratios of a simple disk + powerlaw fit to the before and after (with only a cross-normalization constants free between the model) in Fig. 18, and this reveals the slope change introduced by the new responses. To compare how this slope change affects the source parameters, we used the model: const × TBabs(simplcut × diskbb + relxillNS + xillverCp).

There is a flux increases in FPMA by ∼9%, FPMB by ∼6%, and this is captured almost entirely by an increase in disk normalization of a similar order (∼10%). The shift in spectral slope is more difficult to identify in only one parameter, and it is likely captured by small readjustments of the different model components in the soft band (e.g., relxillNS changes its normalization).

7.2.4 *Cygnus X-1*

The observation of the black hole binary Cygnus X-1 was performed on August 2018 (obsID 80502335002). It constitutes as a bright source in NuSTAR of about ∼250 cts/s, and the model used here for the comparison is: constant × TBabs × (diskbb + cutoffpl + relxill), and the observed differences for the model are:

1. $T_{\rm in}$ (temperature of diskbb model) : $0.41^{+0.04}_{-0.03} \rightarrow 0.53^{+0.07}_{-0.05}$
2. diskbb norm : $11228^{+12993}_{-6107} \rightarrow 2185^{+2157}_{-1100}$

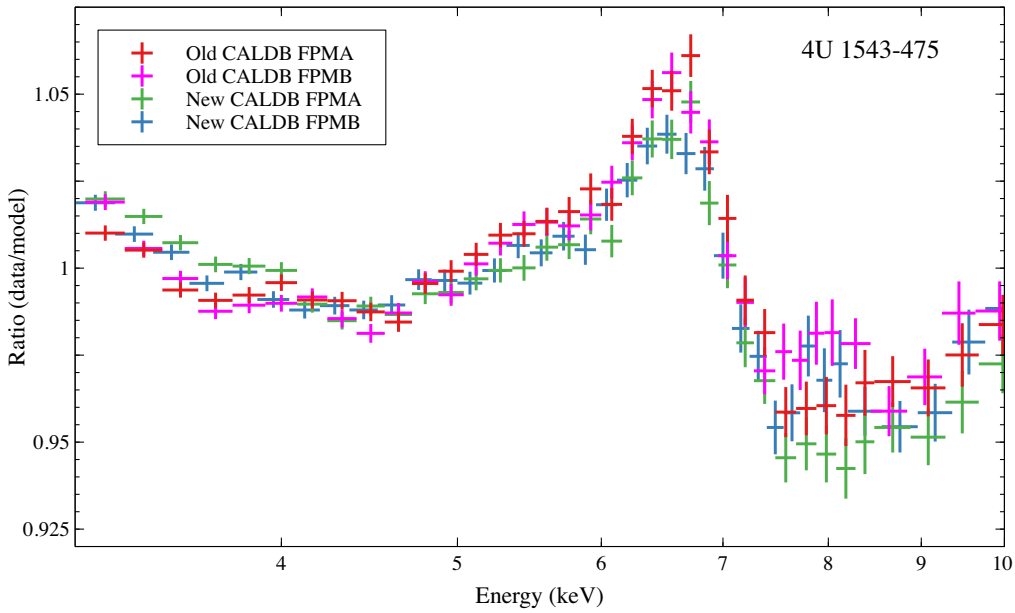

Fig. 18 Ratio plot of data extracted with v007 and v008 ARFs demonstrating the slope shift in the continuum.

3. $\Gamma: 1.74^{+0.01}_{-0.03} \rightarrow 1.71 \pm 0.02$
4. iron abundance: $4.6^{+0.9}_{-0.2} \rightarrow 5.7 \pm 1.0$
5. inclination (deg): $40^{+1}_{-3} \rightarrow 34^{+3}_{-1}$.

We note that the slope and flux difference in the data set, which is induced by the differences in the responses, is once again mostly compensated for in diskbb.

8 Conclusion

In this paper, we have presented a new calibration for NuSTAR released in the CALDB update 20211020. This release includes changes to the vignetting function for both telescopes, the DETABS parameters, and the RMF of all eight detectors. The updated responses were calibrated against the Crab spectral parameters, $\Gamma \equiv 2.103$ and $N \equiv 9.69$, obtained from NuSTAR SL observations, and are a change from the previous calibration performed against $\Gamma \equiv 2.1$ and $N \equiv 8.5$. This results in a model flux increase of 14%, however, due to an off-axis angle dependency to the flux in the previous calibration, the increase observed is 5% to 15%. The new responses significantly improve the response for high off-axis angles ($>4'$) and better agreement between the fluxes and slopes measured by FPMA and FPMB.

We summarize here a set of general changes that may be seen when applying the new CALDB to old data:

1. A flux increase of 5% to 15% depending on off-axis angle.
2. The new RMFs have been calibrated down to 2.2 keV to ensure that the data at 3 keV is resistant to redistribution errors from lower energy but data should still only be fitted down to 3 keV.
3. Significant effective area changes can move power-law slopes around by 0.04 depending on off-axis angle.
4. More accurate high-energy and high off-axis angle corrections.
5. Better FPMA v. FPMB agreement in flux.

The re-analysis of several observations with the new calibration reflects the flux change, and though the new responses caused a minor reshuffling of fitted parameters, none resulted in a new interpretation of the data. The instruments systematic errors have not changed considerably since it was reported on Ref. 4 and we summarize them here:

1. The valid fitting range remains 3 to 79 keV.
2. The expected cross-normalization between FPMA and FPMB is roughly unity with deviations on the order of $\pm 3\%$, but larger values do occur and are usually associated with proximity to detector gaps.
3. There are still residuals that remain in the Crab spectrum. At energies below 30 keV (where statistical errors are insignificant), these are typically at the $\pm 2\%$ level. Above 30 keV, we are limited by the count statistics, and we see residuals on the order of 5% to 10% up to 60 keV and at the 15% level above 60 keV.
4. The systematic errors for power-law slope and flux for repeated observations between $1'$ and $4'$ is $\pm\sigma_\Gamma = 0.01$.
5. The instrument systematic error on the absolute normalization with respect to the Crab was discussed in Ref. 17 and remains 4%.

We emphasize that the calibration updates discussed here do not alter how NuSTAR data is reduced, and that the general steps outlined in the analysis guide[29] remains valid.

Acknowledgments

This work was supported under NASA (Contract No. NNG08FD60C), and made use of data from the NuSTAR mission, a project led by the California Institute of Technology, managed by

the Jet Propulsion Laboratory, and funded by the National Aeronautics and Space Administration. This research has made use of the NuSTAR Data Analysis Software (NuSTARDAS) jointly developed by the ASI Space Science Data Center (SSDC, Italy) and the California Institute of Technology (USA). This material is based upon work supported by NASA (award number 80GSFC21M0002). We thank Murray Brightman, Renee Ludlam, Guglielmo Mastroserio, and Riley Connors for performing the case study re-analyses in Sec. 7.2.

References

1. F. A. Harrison et al., "The Nuclear Spectroscopic Telescope Array (NuSTAR) high-energy X-ray mission," *Astrophys. J.* **770**, 103 (2013).
2. R. Petre and P. Serlemitos, "Conical imaging mirrors for high-speed x-ray telescopes," *Appl. Opt.* **24**, 1833–1837 (1985).
3. K. K. Madsen et al., "Optimizations of Pt/SiC and W/Si multilayers for the nuclear spectroscopic telescope array," *Proc. SPIE* **7437**, 743716 (2009).
4. K. K. Madsen et al., "Calibration of the NuSTAR high-energy focusing X-ray telescope," *Astrophys. J. Suppl. Ser.* **220**, 8 (2015).
5. A. Toor and F. D. Seward, "The Crab Nebula as a calibration source for X-ray astronomy," *Astron. J.* **79**, 995–999 (1974).
6. M. G. Kirsch et al., "Crab: the standard x-ray candle with all (modern) x-ray satellites," *Proc. SPIE* **5898**, 589803 (2005).
7. K. K. Madsen et al., "Measurement of the absolute crab flux with NuSTAR," *Astrophys. J.* **841**, 56 (2017).
8. K. K. Madsen et al., "NuSTAR low energy effective area correction due to thermal blanket tear," arXiv:2005.00569 (2020).
9. "NuSTAR data analysis software and calibration history," https://nustarsoc.caltech.edu/NuSTAR_Public/NuSTAROperationSite/software_calibration.phphttps://nustarsoc.caltech.edu/NuSTAR_Public/NuSTAROperationSite/software_calibration.php (2022).
10. J. E. Koglin et al., "First results from the ground calibration of the NuSTAR flight optics," *Proc. SPIE* **8147**, 81470J (2011).
11. N. F. Brejnholt et al., "NuSTAR on-ground calibration: II. Effective area," *Proc. SPIE* **8443**, 84431Y (2012).
12. N. J. Westergaard et al., "NuSTAR on-ground calibration: I. Imaging quality," *Proc. SPIE* **8443**, 84431X (2012).
13. E. Jourdain and J. P. Roques, "The high-energy emission of the Crab Nebula from 20 keV TO 6 MeV with integral SPI," *Astrophys. J.* **704**, 17–24 (2009).
14. M. C. Weisskopf et al., "On calibrations using the Crab Nebula and models of the nebular X-ray emission," *Astrophys. J.* **713**, 912–919 (2010).
15. C. A. Wilson-Hodge et al., "When a standard candle flickers," *Astrophys. J. Lett.* **727**, L40 (2011).
16. N. Shaposhnikov et al., "Advances in the RXTE proportional counter array calibration: nearing the statistical limit," *Astrophys. J.* **757**, 159 (2012).
17. K. K. Madsen et al., "Observational artifacts of nuclear spectroscopic telescope array: ghost rays and stray light," *J. Astron. Telesc. Instrum. Syst.* **3**, 044003 (2017).
18. J. Wilms, A. Allen, and R. McCray, "On the absorption of X-rays in the interstellar medium," *Astrophys. J.* **542**, 914–924 (2000).
19. D. A. Verner et al., "Atomic data for astrophysics. II. New analytic FITS for photoionization cross sections of atoms and ions," *Astrophys. J.* **465**, 487 (1996).
20. D. R. Wik et al., "NuSTAR observations of the bullet cluster: constraints on inverse compton emission," *Astrophys. J.* **792**, 48 (2014).
21. R. Krivonos et al., "NuSTAR measurement of the cosmic X-ray background in the 3-20 keV energy band," *Mon. Not. R. Astron. Soc.* **502**, 3966–3975 (2021).
22. "NuSTAR SAA filtering reports," https://nustarsoc.caltech.edu/NuSTAR_Public/NuSTAROperationSite/SAA_Filtering/SAA_Filter.phphttps://nustarsoc.caltech.edu/NuSTAR_Public/NuSTAROperationSite/SAA_Filtering/SAA_Filter.php (2022).

23. B. W. Grefenstette et al., "StrayCats: a catalog of NuSTAR stray light observations," *Astrophys. J.* **909**, 30 (2021).
24. G. A. P. Cirrone et al., "Validation of the Geant4 electromagnetic photon cross-sections for elements and compounds," *Nucl. Instrum. Methods Physi. Res. A* **618**, 315–322 (2010).
25. B. W. Grefenstette et al., "Pushing the limits of NuSTAR detectors," *Proc. SPIE* **10709**, 107092V (2018).
26. K. K. Madsen et al., "Broadband X-ray imaging and spectroscopy of the Crab Nebula and Pulsar with NuSTAR," *Astrophys. J.* **801**, 66 (2015).
27. M. Brightman et al., "A luminous X-ray transient in SDSS J143359.16+400636.0: a likely tidal disruption event," *Astrophys. J.* **909**, 102 (2021).
28. R. M. Ludlam et al., "Simultaneous NICER and NuSTAR observations of the ultracompact x-ray binary 4u 1543–624," *Astrophys. J.* **911**, 123 (2021).
29. "NuSTARDAS data analysis quickstart guide," https://heasarc.gsfc.nasa.gov/docs/nustar/analysis/nustar_quickstart_guide.pdf (2022).

Biographies of the authors are not available.